Impact of ultra-low Pt loadings on the performance of anode/cathode in a proton-exchange membrane fuel cell

E. Billy [a,b], F. Maillard [b,*], A. Morin [c], L. Guetaz [c], F. Emieux [a], C. Thurier [d], P. Doppelt [d], S. Donet [a], S. Mailley [e]

[a] CEA, LITEN, Département des Technologies des Nanomatériaux, Laboratoire des Technologies de Surfaces (LTS), 17, Rue des Martyrs, 38054 Grenoble, France
[b] Laboratoire d'Electrochimie et de Physico-chimie des Matériaux et des Interfaces (LEPMI), UMR 5631 CNRS/G-INP/UJF, 1130, rue de la piscine, BP 75, 38402 Saint Martin d'Hères, France
[c] CEA, LITEN, Département des Technologies de l'Hydrogène, Laboratoire des Composants PEM (LCPEM), 17, Rue des Martyrs, 38054 Grenoble, France
[d] Laboratoire d'Ingénierie des Matériaux et des Hautes Pressions (LIMHP), Institut Galilée 99, avenue Jean-Baptiste Clément, 93430 Villetaneuse, France
[e] CEA, DTNM/Laboratoire des Composants pour l'Energie (LCE), 17, Rue des Martyrs, 38054 Grenoble, France

ARTICLE INFO

ABSTRACT

This study focuses on the elaboration of PEMFC electrodes containing ultra-low platinum (Pt) loadings by direct liquid injection metal organic chemical vapor deposition (DLI-MOCVD). DLI-MOCVD offers a large number of advantages for the elaboration of model PEMFC electrodes. First, by using different metal precursors or elaboration temperature, the size of the Pt nanoparticles and thus the intrinsic catalytic activity can easily be tailored in the nanometer range. In this work, Pt nanoparticles (1–5 nm) with remarkable low degree of agglomeration and uniform distribution were deposited onto the microporous side of a commercial gas-diffusion layer (GDL). Second, reduction of the Pt loading is made possible by varying the Pt deposition time and its influence of the cell performance can be extracted without variation of the thickness of the catalytic layer (in previous studies, a decrease of the catalyst utilization was observed when increasing the Pt loading, i.e. the thickness of the catalytic layer (CL)). The electrocatalytic activity of home-made Pt nanoparticles elaborated by DLI-MOCVD was measured in liquid electrolyte or in complete fuel cell operating on H_2/O_2 or H_2/air and compared vs. that of a commercially available electrode containing 500 $\mu g_{Pt}\,cm^{-2}$ (Pt_{Ref500}). At the cathode, the performance of the electrodes containing 104–226 μg of Pt per cm^2 of electrode compares favorably with that of the Pt_{Ref500} in H_2/O_2 conditions. In H_2/air conditions, additional mass-transport losses are detected in the low-current density region but the high effectiveness of our electrodes improves the performance in the high-current density region. At the anode, the Pt loading can be reduced to 35 $\mu g_{Pt}\,cm^{-2}$ without any voltage loss in agreement with previous observations.

© 2009 Elsevier B.V. All rights reserved.

1. Introduction

Proton-exchange membrane fuel cells (PEMFCs) deliver electrical power for stationary or mobile applications [1]. Actually, several scientific hurdles need to be considered to ensure the technological and economic viability of the PEMFC technology. One of the major hurdle is the Pt cost of the membrane electrode assemblies (MEA) [2]. It is usually assumed that classical cathode (400 $\mu g_{Pt}\,cm^{-2}_{geo}$) and anode (200 $\mu g_{Pt}\,cm^{-2}_{geo}$) Pt loadings [2] must be reduced by a factor of at least ten to meet economic viability. The present difference in Pt loading between the two electrodes is due to the sluggish oxygen reduction reaction (ORR) kinetics (the exchange current density of Pt equals $i_0 = 0.05\,A\,cm^{-2}_{Pt}$ [3] at 80 °C−1 bar for hydrogen oxidation reaction (HOR) and $10^{-8}\,A\,cm^{-2}_{Pt}$ [4,5] at ambient pressure and 65 °C for ORR). Since an inexpensive replacement of Pt has not been found yet, Pt must be used to the best and the fullest possible extent.

At the micrometer scale, this implies optimizing the electrode structure/composition to achieve high utilization (u_{Pt}) and effectiveness (ε_{Pt}) factors. The utilization factor u_{Pt} is a measurement of the fraction of the catalyst achieving both ionic and electronic percolation. Experimentally, u_{Pt} is determined as the ratio of the electrochemically active surface area measured in the presence of solid polymer electrolyte to that of the same catalyst but immersed in a liquid electrolyte [2]. In addition to the utilization factor, it is important to quantify the fraction of utilized Pt in the CL under the dynamic conditions of PEMFC operation (ionic or mass-transport limitations). Stonehart and Ross in PAFC [6] and Gloaguen et al.

in PEMFC [7,8] introduced the effectiveness factor ε_{Pt} as the ratio of the experimental current to the intrinsic kinetic current that would have been obtained if there was no mass-transport limitation. Gloaguen et al. [7] showed that ε_{Pt} is a function of the total electrocatalyst area, the electrode thickness and the Nafion® volume fraction and decreases well below 1 for high exchange current densities, high reaction overpotentials or low values of the product DC_s with D the diffusion coefficient and C_s the gas concentration at the catalyst surface. Optimal performance of the CL requires small Pt/C + Nafion® agglomerates (formation of gas pores) and high relative humidity [8]. Using high Pt/C wt.% allows decreasing the thickness of the cathode CL and hence maintaining optimal ionic conduction along the layer thickness [7,9,10]. At the nanometer scale, optimal Pt utilization requires considering the structure sensitivity of the HOR and the ORR (for a review, see [11]) and 3-nm sized Pt particles appear as the best compromise between the specific activity (SA, per real cm^2 of catalyst) and the mass activity (MA, per g of Pt) for the ORR [2,7,10–13]. At the anode, a decrease of the Pt particle size yields an increase of both SA and MA for the HOR [12] but overlap of the diffusion zones between Pt particles impeded high activity of the CL [11].

There are a few studies in the literature which investigated the decrease of the Pt loading on the fuel cell performance. Gasteiger et al. operated 50 and $250\,cm^2$ membrane electrode assemblies under H_2/air or H_2/O_2 at 80 °C. They observed that reducing the anode Pt loading from 400 to $50\,\mu g_{Pt}\,cm^{-2}$ yields voltage losses smaller than 10 mV at the anode [2,14] independently of the oxygen partial pressure. At the cathode, the voltage losses under O_2 are purely kinetic and amount to ca. 20–25 mV when reducing the cathode Pt loading from 400 to $200\,\mu g_{Pt}\,cm^{-2}$. Additional mass-transport losses are predicted when operating under H_2/Air. Passos et al. [15] observed that reduction of the cathode Pt loading below $300\,\mu g_{Pt}\,cm^{-2}$ translates into a decreased Pt electrochemical surface area and impacts negatively the cell performance at 80 °C and 1 bar H_2/O_2. On the other hand, it is worth noting that both groups used catalyst-coated membranes (CCMs) elaborated from spraying or brushing an ink containing an ionomer, a solvent and Pt/C onto the proton-exchange membrane (PEM) [2,14,15]. Hence, an increase of the anode/cathode Pt loading yields an increase of the thickness of the CL, which impacts the effectiveness factor of the electrode. In particular, maintaining optimal ionic conductivity and minimal path length for gas transport/water evacuation is challenging at high thicknesses of the CL. In addition to that, the authors did not focused on optimizing the electrode structure at the nanometer scale: high metal to carbon weight percentages (Pt wt.%) catalyst have been used in these studies to maintain the electrode thicknesses to a reasonable value [2,14] and this is detrimental to the cell performance since Pt particle agglomeration yields low Pt-specific surface area (m^2 per g of Pt) and thus large mass of unutilized Pt. In other words, simultaneous optimization of the electrode structure at both the micrometer and the nanometer scale is impossible with CCM-type electrodes.

In this work, direct liquid injection metal organic chemical vapor deposition (DLI-MOCVD) was utilized to deposit ultra-low Pt loadings on the microporous side of commercial gas diffusion layers (GDL). The home-made electrodes are thus catalyst-coated substrates (CCSs) at variance with the studies conducted by other authors on catalyst-coated membranes [2,14,15]. The electrodes have been characterized using electron-based microscopes. Field emission gun scanning electron microscope (FEG-SEM) images were utilized to determine the volume structure of our electrodes (Pt penetration inside the microporous side of the GDL). Transmission electron microscope (TEM) images taken on the same scale were utilized to build the Pt particle-size distributions. The electrocatalytic activity of the electrodes was determined in liquid
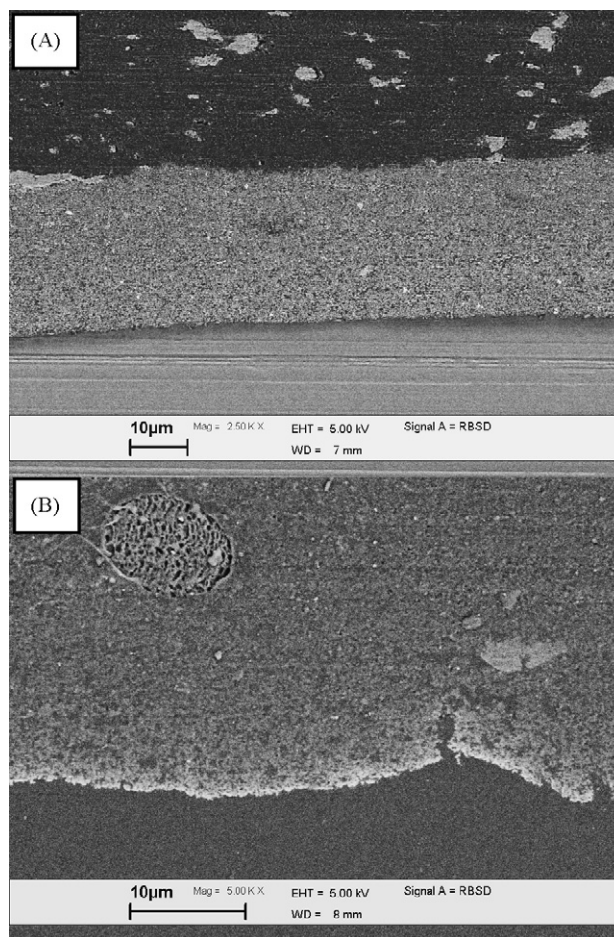

Fig. 1. FEG-SEM images of thin cross-sections of (A) the commercial GDE Pt$_{Ref500}$/C and (B) Pt(cod)$_{60}$/C (Pt nanoparticles loaded at $60\,\mu g_{Pt}\,cm^{-2}$ onto the microporous side of the GDL (see Section 2)). The bottom of the images shows the side facing the PEM. Acceleration voltage 5 kV. Back-scattered electrons detector.

electrolyte (e.g. 0.5 M H_2SO_4) or in solid polymer electrolyte, e.g. in a fuel cell operating on pure H_2/O_2 or H_2/air. A commercially available electrode (ELAT® LT140E-W/SI, BASF Fuel Cell Inc.) with a Pt loading of $500\,\mu g_{Pt}\,cm^{-2}$ was used as a reference material.

2. Experimental

2.1. Preparation of the CL

The gas-diffusion layer GDL used in this work (ELAT® LT1400W, 125 E-TEK BASF) consists of a microporous mixture of carbon particles and polytetrafluoroethylene (PTFE) brushed onto a macroporous carbon cloth through which reactants and reaction products diffuse in and out of the cell. The CL were prepared by depositing Pt nanoparticles by DLI-MOCVD at the carbon microporous side (Fig. 1B) [16–18]. The home-made electrodes are referred indifferently as gas-diffusion electrodes (GDE) or catalyst-coated substrate (CCS). Two different organo-metallic precursors were used: a commercial precursor dimethyl 1,5-cyclooctadiene platinum(II) (Strem, 99%) denoted Pt(cod) hereafter and a home-made precursor denoted Pt(X) [19]. The principle of DLI-MOCVD derives from the conventional chemical vapor deposition (CVD) systems and will be briefly mentioned here. The reactive species (Pt precursors) are solubilized in toluene (Aldrich) and injected with nitrogen at high pressure by injectors (see Fig. 2). By varying the deposition time, five different Pt loadings were achieved: 35, 60, 104, 128 and $226\,\mu g_{Pt}\,cm^{-2}$ (the Pt loading was deter-
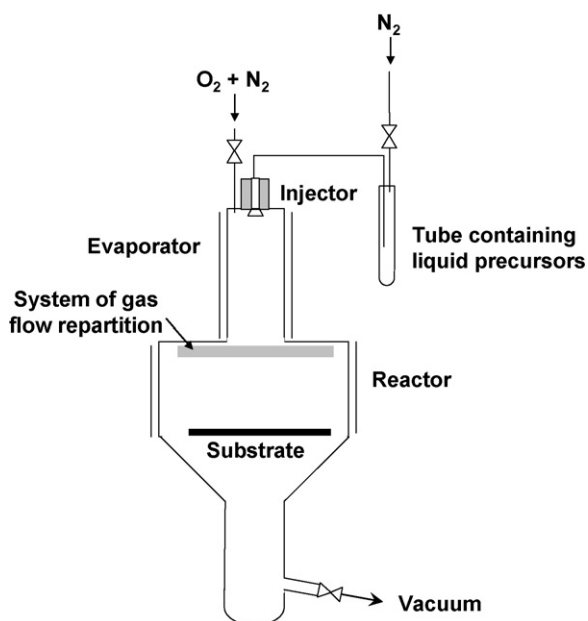
Fig. 2. Schematic representation of the DLI-MOCVD experimental set-up used in this work.

mined by ICP-AES, see Section 2.6). The solvent is evaporated or decomposed by thermal effect and oxidative atmosphere. Precursors are decomposed by the temperature and the gas pressure inside the reactor (Pt(X): 166 Pa and Pt(cod): 800 Pa). Depositions were made under oxidative atmosphere (O_2), at 250 °C for Pt(X) except for Pt(X)$_{104}$/C (300 °C) and 320 °C for Pt(cod) after some preliminary tests to figure out the optimum conditions. The optimum temperature was selected so as to ensure a complete decomposition of the metal precursor and to avoid Pt particle agglomeration induced by high values of temperature. The temperature of the sample holder was identical to that of the reactor. A commercial electrode (ELAT® LT140E-W/SI, BASF Fuel Cell Inc.) containing 500 μg_{Pt} cm^{-2} was used as a reference material (Fig. 1A).

2.2. Measurements in liquid electrolyte

Solutions were prepared from ultrapure water (MQ grade, 18.2 MΩ cm) and sulphuric acid (H_2SO_4 Suprapur, Merck). The glassware was cleaned by soaking in a H_2SO_4:H_2O_2 mixture and thorough washing with ultrapure water before the experiments.

The electrochemical experiments were carried out in 0.5 M H_2SO_4 at room temperature $T = 20 \pm 2$ °C using an Autolab PGSTAT30 potentiostat. Rotating disk electrode (RDE) measurements were performed using a EDI101 Radiometer electrode equipped with a specific Teflon® holder designed to mount/demount easily circular sections (0.28 cm^2) of the home-made electrodes. These sections were deposited onto a glassy carbon disk (Sigradur Grade G) and used as working electrodes. The counter-electrode was a Pt foil whereas the reference electrode was a daily-prepared reversible hydrogen electrode (RHE).

Prior to the measurements, the electrochemical cell was purged with N_2 for 1 h. Then, the potential was swept between 0.05 and 1.00 V at 0.1 V s^{-1} to obtain stable cyclic voltammograms (which normally required ca. 100 potential cycles). Care has been taken to avoid incursions in the region of strong Pt surface oxidation ($E > 1.2$ V vs. RHE). Evaluation of the electrochemically active surface area was made by integration of the current between 0.05 and 0.4 V vs. RHE after substraction of the electrochemical response originating from the carbon support and assuming a charge density

of 210 μC cm^{-2}$_{Pt}$. The specific surface area S_{Hupd} was obtained by dividing the electrochemically active surface area by the platinum mass determined by inductively coupled plasma-atomic emission spectrometry (ICP-AES).

Hydrodynamic voltammograms (at rotation rates varied from 200 to 900 rpm in O_2-saturated solution) for ORR were recorded between 1 and 0.4 V vs. RHE. Prior to each voltammetry, the electrode was kept for 1 min at the starting potential (1 V vs. RHE) to ensure reproducible platinum surface state. The overall ORR current density on the RDE disc is given by the Koutecky–Levich equation [20]:

$$\frac{1}{|i|} = \frac{1}{|i_L^{diff.}|} + \frac{1}{i_K} \tag{1}$$

with

$$\frac{1}{|i_L^{diff.}|} = \frac{1}{|i_L^{diff., solution}|} + \frac{1}{|i_L^{diff., CL}|} \tag{2}$$

where 'i_K' is the kinetic current density, '$i_L^{diff., solution}$' and '$i_L^{diff. CL}$' are the O_2 diffusion limiting current density in the electrolyte and in the active layer, respectively. For RDE experiments, '$i_L^{diff., solution}$' is then expressed from the classical Levich equation [20]:

$$|i_L^{diff., solution}| = 0.62 n F A C_{O_2} D_{O_2}^{2/3} v^{-1/6} \omega^{1/2} \tag{3}$$

where 'n' is the number of electrons exchanged in the electrochemical reaction, F the Faraday's constant, 'A' the surface area, 'C_{O_2}' and 'D_{O_2}' are the concentration and the diffusion coefficient of O_2 in the bulk of the electrolyte, respectively, 'v' the kinematic viscosity and 'ω' the rotation rate in radians per second.

2.3. Measurements in solid electrolyte

To ensure optimal ionic conductivity within the CL while maintaining open porosity for the diffusion of gases, the region of the GDL coated by Pt was impregnated with a diluted Nafion® DE520 suspension supplied by Dupont De Nemours (5 wt.% of ionomer, equivalent weight 1000 g mol^{-1}). The Nafion® loading was equal to the Pt loading for Pt loadings >100 μg cm^{-2}. At Pt loadings <100 μg cm^{-2}, the Nafion loading was 100 μg cm^{-2}. The electrodes were then dried at 80 °C under vacuum for 1 h. When the home-made electrode was tested at the anode, a commercial ELAT® LT140E-W/SI from BASF Fuel Cell Inc. electrode having a Pt loading of 500 g cm^{-2} was used at the cathode and vice versa. A Nafion NRE212 50 μm membrane (Dupont de Nemours®, ca. 1100 g mol^{-1}) was sandwiched at 135 °C and 3.5 MPa between the GDE prepared by DLI-MOCVD and the ELAT® electrode to yield a five-layer MEA. The resulting 25 cm^2 MEA were then assembled into a single cell made of two graphite monopolar plates having a single serpentine flow field channel. The stress applied on the electrodes was controlled to about 1 MPa.

The fuel cell test bench was a commercial CompuCell® GT provided by Globetech. The gas inlet relative humidity is controlled by passing the dry gas through a heated bubbler (the device was previously calibrated to have fully humidified gases at a given temperature). Connection tubes between the single fuel cell and the gas bubbler were heated 15 °C above the single cell temperature in order to avoid condensation prior to the fuel cell inlets. During the data acquisition, the oxygen and hydrogen gas flows are fixed. The GDE were first tested at the anode side and then at the cathode side.

After a standardized start-up procedure, polarization curves were measured by increasing the current density at a rate of 5 mA cm^{-2} s^{-1}. The gases were fully humidified when operating at 80 °C on pure H_2/O_2 with a total pressure P_{tot} H_2/O_2 = 4 absolute bars and stoichiometric flows s = 1.2/1.5, respectively. H_2 and

O_2 gas flows were kept constant at 150 mL min^{-1} for $i < 0.72$ and 1.140 A cm^{-2}, respectively. Above these values, the gas flows were controlled to be proportional to the current density.

The operating conditions were modified for operation at 80 °C on H_2/air. The total pressure P_{tot} H_2/air was 1.5 absolute bars with stoichiometric flows of 1.2 and 2, respectively. The gases were humidified at 50% (inlet). H_2 and air gas flows were kept constant at 150 mL min^{-1} for $i < 0.72$ and 0.17 A cm^{-2}, respectively. Above these values, the gas flows were controlled to be proportional to the current density.

Cyclic voltammetry (CV) were performed using a Biologic VSP potentiostat/galvanostat/impedance with a 20 A/20 V VMP2B booster. The CVs were recorded at 80 °C and 1.5 absolute bars with a sweep rate of 50 mV s^{-1} after the H_2/O_2 polarization curves. The electrochemically active surface area (ESA) was calculated by integrating the charge required to desorb one monolayer of under-potentially deposited H and assuming a charge density of 210 μC cm^{-2}$_{Pt}$.

2.4. FEG-SEM and TEM imaging

For the different electrodes investigated in this work, the distribution of Pt nanoparticles onto the GDL was observed using a LEO 1530 fied emission gun—scanning electron microscope (FEG-SEM). Cross-sections of the MEA have been prepared by ultramicrotomy and observed by transmission electron microscope (TEM) to determine the particle density and size distribution across the thickness of the CL. Ultramicrotomy technique consisted of embedding a small piece of the MEA in an epoxy resin (Struers Epofix) and sectioning thin slices (70 nm) of the embedded sample with a diamond knife at room temperature, using a Leica EM UC6 ultramicrotome. Thin cross-sections were observed with a JEOL 2000FX conventional microscope or a JEOL 4000EX high resolution microscope at an acceleration voltage of 200 and 400 kV, respectively.

The Pt particle-size distribution was reconstructed from the TEM images and utilized for the calculation of the surface average diameter $\bar{d}_S = \sum_{i=1}^{n} n_i d_i^3 / \sum_{i=1}^{n} n_i d_i^2$ and the volume average diameter $\bar{d}_V = \sum_{i=1}^{n} n_i d_i^4 / \sum_{i=1}^{n} n_i d_i^3$ [21]. At least 500 Pt particles have been counted in each case. The surface average mean diameter represents the average diameter of an equivalent sphere (TEM images are 2D projections of 3D objects). The mean crystallite size determined in XRD from the width at half-maximum of the Pt{1 1 1} peak should be compared with the volume average mean-particle size determined by TEM. The fourth power in the equation is difficult to interpret but possess physical significance (see [22]).

2.5. X-ray measurements

X-ray diffraction patterns were recorded using a Bruker D5000 diffractometer with a Cu Kα radiation source operating at 40 kV and 30 mA. The angles were scanned over a range of 15° to 90° at a rate of 5° min^{-1} with an angular resolution of 0.02°. The Determination of the Pt particle size d_{XRD} (Table 1) was performed using the Debye–Scherrer formula from the (1 1 1), (2 0 0) and (3 1 1) diffraction peaks.

2.6. ICP-AES measurements

The Pt content contained in each electrode was measured by inductively coupled plasma-atomic emission spectrometry (ICP-AES, IRIS). Pt/C samples were first digested in concentrated aqua regia (6.6 M HCl – 2.1 M HNO$_3$) made from high purity acids (Suprapur®, Merck) at ca. 60 °C overnight. Part of the digestion solution was then pipetted and diluted so as to obtain a working solution containing 50 ppm of the metal (based on the metal load-

ings indicated by E-TEK) in diluted aqua regia (below 1 M HCl). The Pt loading was averaged from the measurements of 3 Pt-related ($\lambda = 265.945$, 214.423 and 204.937 nm) wavelengths.

3. Results and discussion

3.1. Chemical characterization by ICP-AES

ICP-AES analysis was utilized to determine the exact Pt loading deposited onto each electrode and thus determine the mass activity of the catalysts for the oxygen reduction reaction (ORR). In the rest of this work, the electrodes will be referred as Pt(precursor)$_{loading}$/C where precursor refers to X or cod (see Section 2) and loading refers to the Pt loading determined by ICP-AES (35, 60, 104, 128, 226 μg cm^{-2} for the home-made electrodes and 500 μg cm^{-2} for the commercial electrode, see Section 2).

3.2. Physical characterization

A major concern of the work is to preserve high electrochemical active surface area by avoiding coalescence of the Pt nanoparticles onto the carbon support and favoring their penetration within the volume of the electrode. The presence of Pt nanoparticles within the volume of the electrode is determined by the mobility of the Pt precursor onto the substrate and is strongly impacted by its chemical nature (more precisely its temperature of decomposition), the chemical state/heterogeneity of the substrate, the experimental conditions inside the reactor (chamber pressure, atmosphere and temperature) and the energy required for nucleation/growth. From the FEG-SEM images of Fig. 1B, Pt nanoparticles are still visible at ca. 10 μm from the GDL side facing the PEM. Complementary analysis was performed by cross-sectioning one GDE (Pt(cod) with a metal loading of 60 μg$_{Pt}$ cm^{-2}) by ultramicrotomy and acquiring TEM images. This allows determining the particle density and the size distribution across the thickness of the CL (Fig. 4). At 6 μm from the GDL region facing the PEM, we observed a decrease of the Pt particle density per cm^2 of carbon while maintaining the Pt particle size nearly constant to ca. 3–4 nm. At larger distances (Fig. 3D), the size of the Pt nanoparticles and their density are strongly decreased. We noted that Pt nanoparticles are present at 14 μm from the GDL surface. When comparing our results with those of other groups, it is interesting to note that the Pt deposited by DLI-MOCVD is localized in a small volume. Indeed, the maximal penetration depth observed in this work (ca. 14 μm) differs considerably from the values reported by Brault et al. [23] (ca. 2000 nm) and Cavarroc et al. [24] (ca. 200 nm) for electrodes elaborated by plasma sputtering and loaded to ca less than 100 μg$_{Pt}$ cm^2. A fast calculation demonstrates that 90% of the Pt mass deposited in our electrodes is contained within the first 2–3 μm of the GDL region facing the PEM. Similar observations have been performed for Pt(X) but are not presented here.

Fig. 4 presents FEG-SEM electron images of the Pt nanoparticles deposited on the microporous side of the commercial GDL. For both Pt(cod) and Pt(X) precursors, DLI-MOCVD allows a very uniform coating of the carbon particles by Pt nanoparticles and this is at variance with the commercial electrode used in this work. Fig. 4 also shows the influence of the Pt loading on the morphology of the deposited Pt. Increasing the Pt loading (achieved by increasing the deposition time) results in larger Pt particle sizes. This can be easily understood in the frame of a nucleation-growth-coalescence model where individual Pt islands are first nucleated on the surface and then agglomerate to form larger structures and, ultimately, a dense and continuous Pt thin film. The nanostructure of the Pt nanoparticles (size, density and degree of agglomeration)
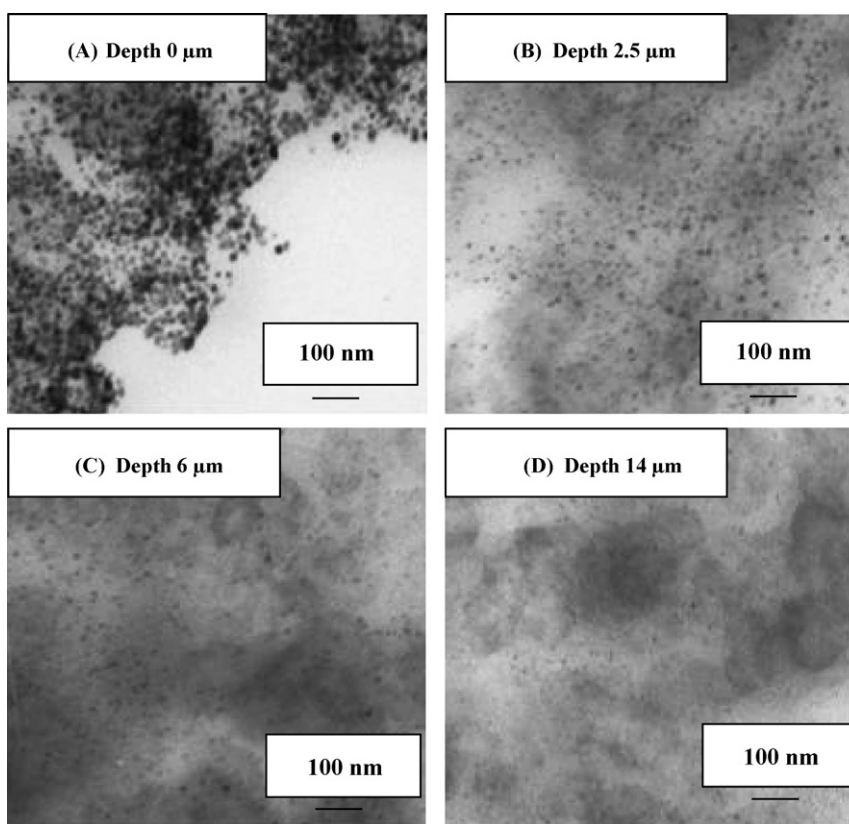
Fig. 3. Thin cross-sections of Pt(cod)$_{60}$/C electrode observed by TEM at different distances from the interface with the PEM. (A) Interface 0 μm, (B) 2.5 μm, (C) 6 μm and (D) 14 μm.
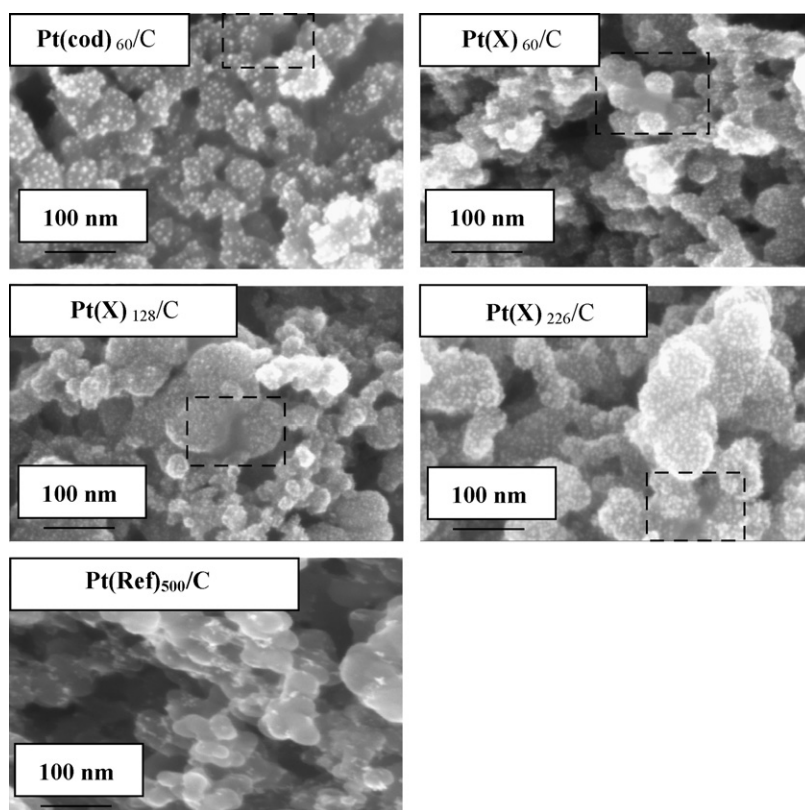

Fig. 4. FEG-SEM images of platinum nanoparticles deposited by DLI-MOCVD on the microporous side of a commercial GDL. A commercial GDE loaded at 500 μg$_{Pt}$ cm^{-2} purchased from BASF (Pt$_{Ref500}$/C) was used as a reference material (see Section 2). Acceleration voltage 5 kV, In-lens detector. Dotted boxes refer to PTFE aggregates present in the GDL.

Table 1

Mean-particle size determined by TEM, XRD and H_{upd} desorption for the electrodes elaborated by DLI-MOCVD and a commercial Pt_{Ref500} electrode (see Section 2). The mean-particle size has been estimated by XRD (d_{XRD}) using Scherrer equation and the {1 1 1}, {2 0 0}, {3 1 1} diffraction peaks of Pt. $\bar{d}_{Hupd}$ is the mean-particle size estimated from electrochemical measurements in 0.5 M H_2SO_4. $MA_{0.85}$ is the mass activity for ORR determined at $E = 0.85$ V vs. RHE at $T = 20$ °C and $PO_2 = 1$ bar in 0.5 M H_2SO_4.

	Electrode loading (m_{Pt} μg_{Pt} cm^{-2}_{geo})	$\bar{d}_S$ (nm)	$\bar{d}_V$ (nm)	$\bar{d}_{XRD}$ (nm)	$\bar{d}_{Hupd}$ (nm)	b/Tafel slope (mV decade^{-1})	$MA_{0.85}$ (A g$_{Pt}^{-1}$)
Relative error	±1	±0.2	±0.2	±0.2	±0.2	±5%	±5%
Electrode Pt(cod)$_{60}$/C	60	4.3	4.6	5.1	3.8	55	74
Electrode Pt(X)$_{60}$/C	60	3.2	3.7	–	3.2	60	118
Electrode Pt(X)$_{128}$/C	128	–	–	1.7	4.5	61	63
Electrode Pt(X)$_{226}$/C	226	5.6	6.4	3.1	6.0	63	48
Electrode Pt$_{ref500}$/C	500	3.7	3.9	4.2	4.6	–	–

deposited by DLI-MOCVD compares favorably with that of Pt thin films deposited on native and thermally oxidized Si [25,26], Pt/NSTF electrodes elaborated by 3 M onto organic whiskers [27,28] or electrodes elaborated by sputtering of Pt onto a GDL [24,29–31]. In particular, special attention has been paid in this work to limit the coalescence of the individual Pt particles. The experimental parameters of choice for that are the deposition temperature, the pressure inside the reactor and the precursor concentration because they all influence the nucleation/surface diffusion rate of Pt precursors/adatoms onto/inside the substrate surface/volume. At low deposition temperatures, the nucleation rate is expected to be large due its Arrhenius-type dependence and the surface diffusion is slow. On the other hand, low deposition temperatures may yield incomplete decomposition of the Pt precursor and thus pollution of the Pt surface sites by carbonated molecules thus affecting negatively the catalytic reactions. In what follows, we show the effect of the temperature on the morphology of the Pt deposits. Instead of using a single precursor and depositing it at different temperatures, we used two different Pt precursors: Pt(cod) decomposing at ca. 180 °C and Pt(X) decomposing at 150 °C (the decomposition temperature of the Pt precursors was established by TGA analysis). Since deposition of Pt(cod) was made at 320 °C and deposition of Pt(X) was made at 250 °C (same precursor concentration, same reactor pressure), any contamination of the Pt catalytic sites by carbonated molecules coming from incomplete decomposition of the metal precursor or oxygen coming from the reactor atmosphere can be ruled out. In a previous paper, Goswami et al. [26] noticed less than 1 at.% carbon and oxygen contamination when depositing Pt(acac)2 at comparable substrate temperature (350 °C) and reactor pressure (3.5 bars). Finally, we notice that larger Pt particles with lower density per cm^2 of carbon are formed when using Pt(cod) rather than Pt(X) in agreement with the above. We have also detected a minority of Pt-uncovered zones (see Fig. 4 dotted boxes), which we believe are PTFE aggregates present in the GDL.

In Fig. 5, we plotted the Pt particle-size distributions obtained for Pt(cod)$_{60}$/C, Pt(X)$_{60}$/C and the commercial Pt$_{Ref500}$ electrodes reconstructed from TEM images taken at the same scale. Pt nanoparticles elaborated by DLI-MOCVD possess small particle sizes (1–5 nm) with low degree of agglomeration and uniform distribution onto the carbon particles. We noticed that smaller Pt nanoparticles are elaborated with Pt(X) vs. Pt(cod) or the commercial Pt$_{Ref500}$ electrode, which is likely related to different temperatures of decomposition of the metal precursor. The mean-particle sizes determined by TEM, XRD and H_{upd} desorption are compared in Table 1. In XRD, the average crystallite size $\bar{d}_{XRD}$ was determined using the Debye–Scherrer equation and the {1 1 1}, {2 0 0}, {3 1 1} diffraction peaks of Pt. $\bar{d}_{XRD}$ compares fairly with the volume average mean-particle size $\bar{d}_V$ determined by TEM, translating the fact that Pt/C nanoparticles are single crystallites (the size of coherently scattering domains agrees with the particle size determined by TEM) and that the fraction of agglomerated particles

is small. There is also a good agreement between the mean-particle sizes $\bar{d}_S$ and $\bar{d}H_{upd}$ determined from TEM or from electrochemical measurements, respectively. This confirms that 100% of the Pt particles contained within the CL are in contact with the liquid electrolyte and that surface contamination can be ruled out. An increase in the Pt loading yields an increased $\bar{d}_{H_{upd}}$, reflecting the coalescence of Pt particles which was also observed by FEG-SEM (Fig. 4).

3.3. Electrocatalytic activity in liquid electrolyte

In Table 1, we report the mass activity (MA) for the ORR of GDE elaborated with Pt(cod) and Pt(X) at a constant Pt loading of 60 μg_{Pt} cm$^{-2}_{geo}$ or with Pt(X) at but different loadings varying from 60 to 226 μg_{Pt} cm$^{-2}_{geo}$. We start with the effect of the Pt loading on the electrocatalytic activity for the ORR. As previously shown in Section 3.2 and Table 1, an increase of the Pt loading yields to an increase of the Pt particle size and thus a decrease of the specific surface area (cm^2 g$_{Pt}^{-1}$). In terms of electrocatalytic activity, decreasing the Pt particle size from ca. 10 to 3–4 nm results in a decrease of the specific activity SA (per real cm^2 of Pt) and a pronounced increase of MA (per g of Pt) [2,7,10,11]. For Pt particle sizes below 3–4 nm, the increase in specific surface area is counterbalanced by the rapid decrease of SA yielding an optimum for
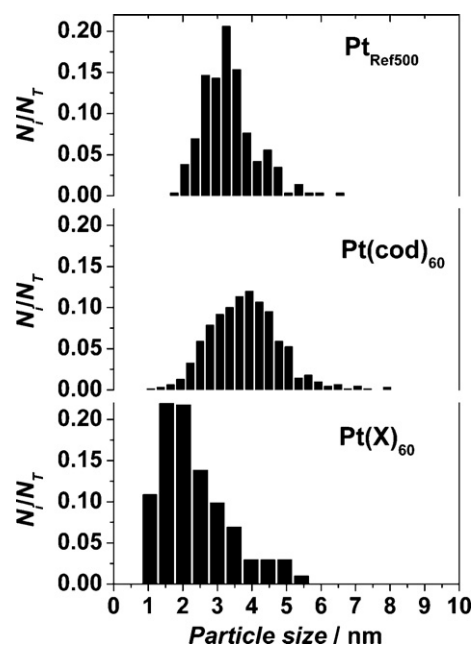

Fig. 5. Particle-size distributions reconstructed from TEM images for three electrode materials used in this work. The TEM images contained a small fraction of agglomerated or non-spherical Pt particles, which were not considered in the particle-size distribution. At least 500 particles have been counted in each case.
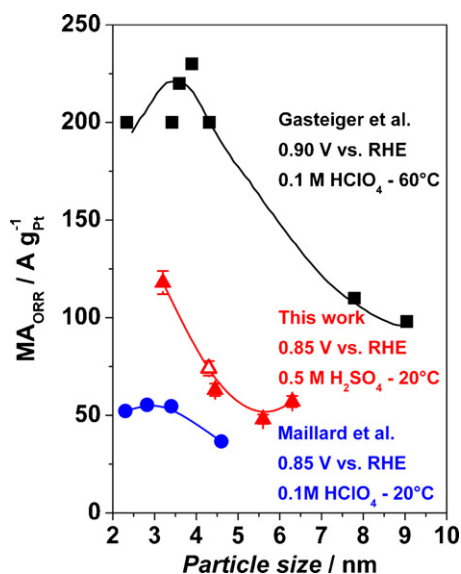
Fig. 6. Mass activity (A g_{Pt}^{-1}) for the ORR in oxygen-saturated liquid acid electrolyte vs. the particle size of Pt/C. (filled squares) Pt/Vulcan XC-72 in 0.1 M HClO₄ at 0.9 V vs. RHE at 60 °C [3], (filled circles) Pt/Vulcan XC-72 in 0.1 M HClO₄ at 0.85 V vs. RHE at 20 °C [11], (filled triangles) Pt(X) in 0.1 M H₂SO₄ at 0.85 V vs. RHE at 20 °C and (opened triangle) Pt(cod) in 0.1 M H₂SO₄ at 0.85 V vs. RHE at 20 °C (the values are reproduced from Refs. [2,10] with the permission of Elsevier).

MA. This trend is illustrated in Fig. 6, which compares MA as a function of the Pt particle size for the catalysts elaborated in this work and for commercial catalysts [2,10]. Our results agree with the structure sensitivity of the ORR observed in perchloric acid by other groups [2,10]. When comparing the electrocatalytic activity of Pt(cod) and Pt(X) at a constant Pt loading of 60 μg_{Pt} cm^{-2}, we found superior MA for Pt(X) vs. Pt(cod) (Table 1). Similarly to what was explained previously, this can be accounted for by different Pt particle sizes resulting from different temperatures used during the elaboration of the GDE. It is also interesting to note that the decomposition of the precursor was complete and that no pollution of the catalytic sites should be assumed (MA values for Pt(cod) and Pt(X) are fitted nicely by the same curve in Fig. 6).

A major conclusion from this part is that not only the mass of Pt loaded onto the GDL but also its nanostructure plays a key-role on the MEA performance (and thus the Pt cost per kW). Indeed, it is interesting to consider the particle-size distribution of Pt(cod)₆₀/C. An area and a volume distribution of Pt particles were built assuming hemispherical Pt particle shapes (this approximation is very classical in the literature, see Ref. [22]). It appeared that only one sixth of the largest particles ($d > 4.9$ nm) represents one half of the total mass of platinum loaded onto the electrode but contributes only for one fifth to the electrochemically available surface area.

Hence, there are obvious industrial interests to use metal precursors decomposing at smaller temperatures in DLI-MOCVD: (i) lower temperature of elaboration and (ii) maximization of the Pt surface/mass ratio. In the rest of this study, we have focused our efforts on the Pt(X) precursor.

3.4. Electrochemical activity in solid polymer electrolyte

3.4.1. Utilization factor u_{Pt}

Table 2 compares experimental values of the specific surface area determined by integration of the H_{upd} desorption charge (after subtraction of the electrochemical response from the C support and assuming a charge density of 210 μC cm^{-2}$_{Pt}$) at 100 mV s^{-1} in liquid electrolyte, S_{Hupd} or at 50 mV s^{-1} in solid polymer electrolyte, $S_{Hupd,MEA}$. A good agreement is obtained between the values determined in both electrolytes. This points towards full utilization of the catalyst deposited by DLI-MOCVD in the solid polymer electrolyte (full accessibility of the Pt particles in liquid electrolyte has been demonstrated by comparing the mean-particle size determined by TEM $\bar{d}_S$ and by electrochemistry $\bar{d}H_{upd}$, see Section 3.2). High values of $S_{Hupd,MEA}$ translate into utilization factors $u_{Pt} = (S_{Hupd,MEA}/S_{Hupd})$ close to 100% for Pt loadings larger than 226 μg cm^{-2} or exceed 100% for Pt loadings below 226 μg cm^{-2}, which indicates under-estimation of S_{Hupd} or overestimation of $S_{Hupd,MEA}$. Since the mean-particle sizes found by integration of the H_{upd} charge in liquid electrolyte agree with those found by TEM, we believe the second hypothesis is the most plausible. Indeed, decreasing the Pt loading and hence the Pt particle size yields large uncertainties in the determination of the surface area via the H_{upd} charge. In particular, correction of the electrochemical response originating from the carbon support becomes to a large extent difficult at such low Pt loadings. In addition to that, the higher acidity of the electrolyte (Nafion® in the MEA vs. 0.5 M sulphuric acid-soaked reconstituted Nafion® in RDE experiments) shifts the H_{upd} adsorption/desorption region towards more negative potentials. Hence, when using the same negative potential limit of 0.05 V vs. RHE in fully humidified solid electrolyte and in liquid electrolyte, H₂ evolution can be observed in the former case but not in the latter. The produced H₂ is easily oxidized on the positive-going potential scan and the electrochemically surface area $S_{Hupd,MEA}$ becomes severely overestimated. We have also observed that H₂ evolution is facilitated by a decrease of the Pt particle size that is a decrease of the Pt loading.

Despite large uncertainties associated with the reduction of the Pt loading, u_{Pt} values are close to 100% at high Pt loadings and compare favorably with those found in the literature. The first reason for that is believed to be the particular geometry of our Pt-coated GDL. Indeed, it is well-established that CCM electrodes present random distribution of the CL components: gas pores, Pt/C and ionomer and thus result in incomplete utilization of the electrocatalyst [2,32–35]. In randomly distributed CCM electrodes, a
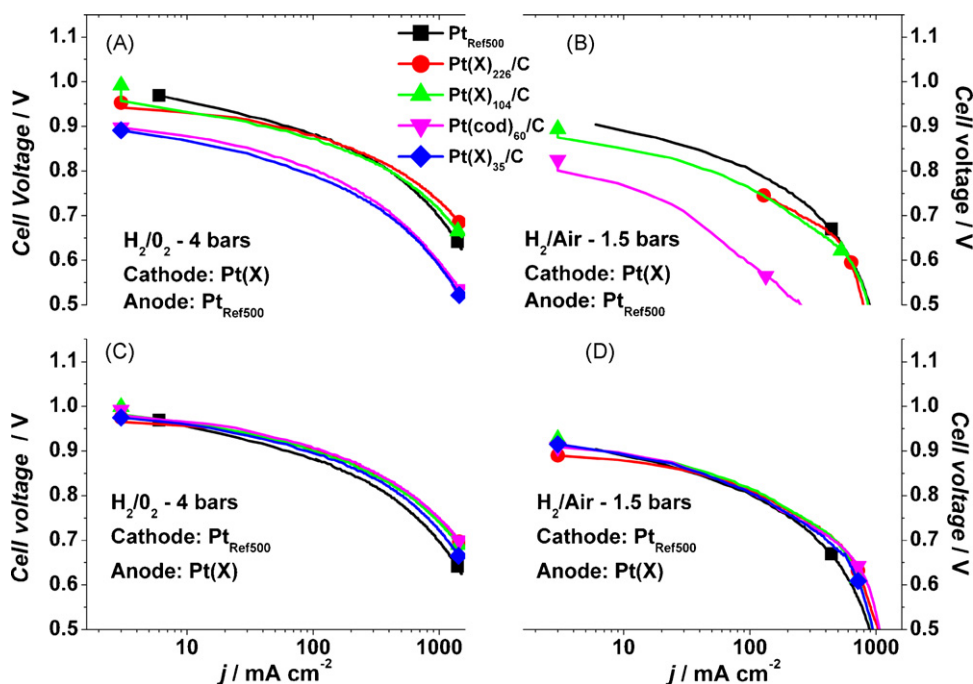
Table 2

Pt specific surface areas for the MEA cathodes and their roughness factors determined in liquid electrolyte (e.g. 0.5 M H₂SO₄) or in solid electrolyte (e.g. in real fuel cell) using fully humidified H₂ (anode) and N₂ (cathode). A charge density of 210 μC cm^{-2}$_{Pt}$ has been assumed. The utilization factor u_{Pt} is defined as the ratio of the electrochemically active surface area measured in the presence of solid polymer electrolyte to that of the same catalyst but immersed in a liquid electrolyte.

Catalyst	Liquid electrolyte		Solid polymer electrolyte		u_{Pt} (%)
	RF_{elec} (cm²$_{Pt}$ cm^{-2}$_{geo}$)	S_{Hupd} (m² g^{-1}$_{Pt}$)	RF_{elec} (cm²$_{Pt}$ cm^{-2}$_{geo}$)	$S_{Hupd,MEA}$ (m² g^{-1}$_{Pt}$)	
Relative error	±5	±5	±5	±5	±10
Pt(cod)₃₅C	31	87	63	209	240
Pt(X)₃₅/C	39	112	–	–	–
Pt(X)₁₀₄/C[a]	66	63	82	79	125
Pt(X)₁₂₈/C	80	63	–	–	–
Pt(X)₂₂₆/C	106	47	107	47	100
Pt₍Ref500₎/C	303	61	308	62	101

[a] Elaborated at 300 instead of 250 °C.

Fig. 7. Polarization curves of the MEAs elaborated in this work for 25 cm^2 single cells. MEAs based on Pt(X)/C or Pt(cod)/C at different Pt loadings or a commercial Pt$_{Ref500}$/C loaded at 500 μg$_{Pt}$ cm^{-2}$_{geo}$. Membrane NRE212 50 μm (EW ca. 1100 g mol^{-1}). Ionomer Nafion® DE520 (5 wt.% of ionomer, EW 1000 g mol^{-1}). T_{cell} = 80 °C. The MEA operated with fully humidified gases at P_{tot} H$_2$/O$_2$ = 4 absolute bars with stoichiometric flows s = 1.2/1.5, respectively or at P_{tot} H$_2$/air = 1.5 absolute bars with stoichiometric flows s = 1.2/2, respectively, with gases humidified at 50% (inlet).

maximum utilization factor u_{Pt} of 0.22 and 0.4 has been predicted by Farhat [35] and Eikerling and Kornyshev [32,33], respectively. Experimentally, Gasteiger et al. [2] found that the catalyst utilization is strongly dependent on the MEA preparation conditions and may vary between 0.75 and 0.98. Improving the catalyst utilization u_{Pt} may be achieved by introducing spatial order in the CL. The most relevant example was achieved by Debe [28]. The authors evidenced that u_{Pt} may approach 1 for electrodes based on oriented crystalline organic whiskers coated by a nanostructured Pt thin film (Pt/NSTF). The Pt thin film forms a continuous network providing electronic conduction via Pt and ionic conduction via proton transport in the voids located between different whiskers. In this work, we have elaborated CCS electrodes containing small Pt loadings in which 90% of the Pt particles are located within the first 2–3 μm of the microporous side of the GDL. The ionomer was incorporated afterwards on the catalyst-coated substrate by immersion of the GDE into a diluted Nafion® solution according to a procedure previously developed by Cheng et al. [36]. The GDE were then hot-pressed onto the PEM (favoring penetration of the CL inside the PEM) so as to improve the ionic percolation and reach high u_{Pt}. Hence, the small dimension of the CL (2–3 μm), the precise localization of the catalyst onto the carbon support, the coating of the Pt nanoparticles by an ionomer film and the hot-pressing step are numerous experimental parameters that reasonably account for the observed high values of u_{Pt}.

Fig. 7A and B displays the $U(j)$ performance of MEA composed of the Pt(X) and Pt(cod) electrodes elaborated by DLI-MOCVD at the cathode and Pt$_{Ref500}$ at the anode. Fig. 7C and D displays the $U(j)$ performance of the same electrodes at the anode with Pt$_{Ref500}$ at the cathode. We tested two possible configurations: 80 °C – 4 bars H$_2$/O$_2$ pressures – 100% RH providing negligible reactant depletion and water accumulation through the CL and thus raising the electrical performance of the MEA (Fig. 7A and C) and 80 °C – 1.5 bars H$_2$/air pressures – 50% RH, which are more realistic of electric vehicle applications (Fig. 7B and D).

3.4.2. Effect of the Pt loading on the performance of the cathode

We start with the electrodes elaborated by DLI-MOCVD at the cathode of the PEMFC. It is common practice to associate the voltage losses observed in the polarization curves to different components [2]. At low current densities, voltage losses are ascribed to the sluggish ORR kinetics and are thus affected by a variation of the electrochemical Pt surface area. At intermediate current densities, Ohmic losses are generated by the proton resistance in the catalytic layers/PEM and the contact resistances between the flow-fields plates and the diffusion media. At high-current densities, mass-transport losses are induced by poor gas transport into the diffusion media/CL.

At 4 bars O$_2$ pressures, the performance of the electrodes containing 104–226 μg$_{Pt}$ cm^2 is nearly superposed with that of the Pt$_{Ref500}$ in the region $0 < j < 0.5$ A cm^{-2}. The kinetic losses observed upon decreasing the Pt loading from 500 to 226/104 μg of Pt per cm^2 are smaller than those predicted by Gasteiger et al. on the basis of a Tafel slope of 65 mV per decade of Pt loading [14]. This can be rationalized by considering different Nafion:C contents [15] and different electrode preparation techniques used in this work and in other works [2,14]. Whereas reduction of the Pt loading in CCM-type electrodes results in identical Pt-specific surface area (cm^2 g$_{Pt}$$^{-1}$) but a pronounced decrease of the electrode roughness RF$_{elec}$ (cm^2$_{Pt}$ cm^{-2}$_{geo}$), elaboration of Pt nanoparticles by DLI-MOCVD yields an increase in Pt-specific surface area (see Table 2), which may counterbalance RF$_{elec}$. At low current densities ($j < 0.3$ A cm^{-2}) and considering that the cathode fix the cell performance, the polarization curves are adequately fitted by apparent Tafel slopes b of ca. 50–70 mV decade^{-1} whatever the metal loading (not shown). This confirms previous observations of Gasteiger et al. that kinetics losses dominate the MEA performance up to 1 A cm^{-2} in H$_2$/O$_2$ conditions [9,14]. The values of the apparent Tafel slope also agree with those found in solid polymer [9,14,15,37] or in liquid electrolyte (Table 1 and [2,7,10,38]) on commercial Pt/C nanoparticles. Interestingly, the value of the Tafel slope b decreases slightly
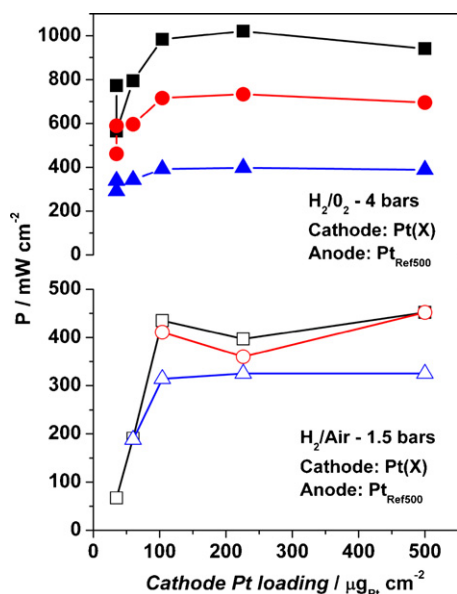
Fig. 8. Maximal power density (squares), power density at 1 A cm^{-2} (circles) and power density at 0.5 A cm^{-2} (triangles) as a function of the cathode Pt loading at 80 °C in H$_2$/O$_2$ conditions at a total pressure of 4 bars (filled symbols) or in H$_2$/air conditions at a total pressure of 1.5 bars (opened symbols). Other conditions, see Fig. 7.
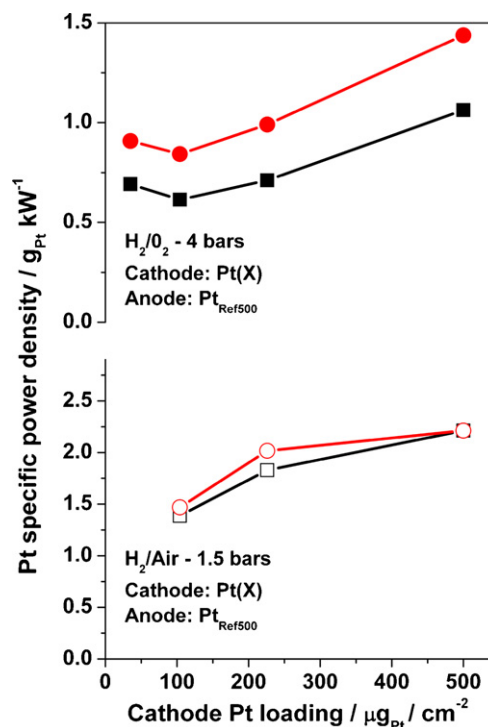

Fig. 9. Platinum specific power density obtained for the maximum power density P_{max} (squares) and obtained at 1 A cm^{-2} (circles) for different cathode Pt loadings elaborated with the Pt(X) precursor. Tests were performed at 80 °C in H$_2$/O$_2$ conditions at a total pressure of 4 bars (filled symbols) or in H$_2$/air conditions at a total pressure of 1.5 bars (opened symbols). Other conditions, see Fig. 7.

upon decreasing the Pt loading in both liquid (see Table 1) and solid polymer electrolytes (not shown), which may indicate different surface coverages of Pt nanoparticles by oxygenated species or an increased contribution of the C support to the ORR kinetics. In the frame of the first explanation, it is worth noting that two linear regions with a slope of −60 mV decade^{-1} at high potentials (where Pt is partially covered by oxygenated species) and −120 mV decade^{-1} at low potentials (where Pt is oxide free) are usually observed in ORR Tafel plots. Hence, a decrease of the Tafel slope b with decreasing the Pt loading (and hence the Pt particle size) would point towards an increased coverage of Pt nanoparticles by oxygenated species in agreement with XANES observations of Mukerjee and Mac Breen [39]. In the frame of the second explanation, a single Tafel slope of ca. 40 mV decade^{-1} was observed by Genies et al. [40] in alkaline solution on pure C powder. Hence, lower values of the Tafel slope with decreasing the Pt loading may be accounted for by the higher contribution of C to the ORR kinetics. However, considering the potential region in which O$_2$ reduction is initiated on C in acidic medium ($E < 0.85$ V vs. RHE [41]) and the potential region in which the Tafel slope has been determined here (0.95 – 0.85 V vs. RHE), this explanation appears very unlikely. Finally, we notice that electrodes containing Pt loadings greater than 104 µg of Pt per cm^2 outperform the performance of the Pt$_{Ref500}$ at current densities larger than 0.35 A cm^{-2}, with no traces of mass-transport limitations up to 1.5 A cm^{-2}. Since all electrodes are of CCS type, this signs better catalyst effectiveness of home-made electrodes compared to the Pt$_{Ref500}$, most likely caused by the "optimized" cathode structure (localized spatial distribution of Pt particles, gas voids and ionomer in this work vs. random distribution in the commercial Pt$_{Ref500}$). In terms of electrical performance, the cell voltages found in this work (4 bars H$_2$/O$_2$, 100% RH, 80 °C) agree with those found by Hirano et al. (5 atm H$_2$/O$_2$, 95 °C) with cathodes elaborated by sputtering Pt directly onto the GDL [30].

Contrary to the H$_2$/O$_2$ performance, additional mass-transport losses affect the 1.5 bars H$_2$/air polarization curves in the low-current density region ($j < 0.2$ A cm^{-2}). The small thickness (2–3 µm) of our catalytic layer and the sluggish ORR kinetics are

likely contributing to facile formation of N$_2$ plugs and water flooding at close proximity of the Pt nanoparticles resulting in higher mass-transport resistances and decreased electrical performance. Due to the greater effectiveness of our home-made electrodes, the electrical performances become comparable at current densities larger than 0.75 A cm^{-2} for Pt loadings greater than 104 µg$_{Pt}$ cm^{-2}.

3.4.3. Effect of the Pt loading on the performance of the anode

Fig. 7C and D shows a slight decrease of the reversible potential when decreasing the Pt loading from 226 to 35 µg$_{Pt}$ cm^{-2} in agreement with previous observations of Gasteiger et al. [2] and Cunningham et al. [42]. Interestingly, home-made anodes perform better than the Pt$_{Ref500}$ electrodes over the whole range of current densities explored in this work and changing the gas pressure from 4 to 1.5 bars does not affect this trend. It appears also essential to compare the performance of our GDE with those obtained by other groups using similar thin film deposition techniques. In a recent study, Caillard et al. [43] observed that 5–100 µg$_{Pt}$ cm^{-2} anodes prepared by plasma sputtering yield comparable cell performances than Pt$_{Ref500}$ in the low-current density region (<0.5 A cm^{-2}) and at high gas pressures (3 bars). However, decreased cell performance vs. Pt$_{Ref500}$ was observed when increasing the current density or decreasing the gas pressure. Since Pt deposition was performed on identical ELAT® GDLs and that the same reference material Pt$_{Ref500}$ was used in both studies, it is important to understand the origin of those differences. First, this may be related to the accumulation of water in the GDE. However, the Nafion® content of the electrodes elaborated by Caillard et al. had been previously optimized on the basis of the highest cell performance [43], and thus such effect appears very unlikely. The second explanation might be the low roughness factors of the electrodes. Indeed, SEM images of the Pt/C electrocatalysts presented in Ref. [43] revealed carbon particles covered by agglomerated Pt nanoparticles, the size of which varies between 5 and 20 nm (see Fig. 2 in Ref. [43]). It is worth not-

ing that the agglomeration degree of the Pt particles increases with increasing the thickness of the deposited Pt film, i.e. the Pt loading. Hence, decreased values of RF_{elec} may induce large kinetic losses, which will dominate the cell performances. At variance with the work of Caillard et al. [43], special care has been taken in this work to elaborate highly dispersed Pt nanoparticles with low degree of agglomeration.

As a conclusion, this study shows that it is possible to use Pt loadings as low as 35 μg_{Pt} cm^{-2} at the anode without any voltage loss in agreement with previous works [2,14,42]. At the cathode, the electrodes elaborated by DLI-MOCVD perform better than the commercial Pt$_{Ref500}$ electrode at current densities larger than 0.35 A cm^{-2} in conditions providing negligible reactant depletion and water accumulation through the CL (80 °C – 4 bars H$_2$/O$_2$ pressures – 100% RH). Concomitant to the reduction of the Pt loading, the decrease of the mean Pt particle size yields an optimum in power density for Pt loadings of ca. 225 μg cm^{-2} (see Fig. 8). It induces a Pt-specific power density of 0.6 g_{Pt} kW^{-1} (see Fig. 9), that is promising given the non-optimized anode Pt loading (500 μg cm^{-2}). In H$_2$/air conditions, additional mass-transport losses appear, most likely due to N$_2$/O$_2$ transport through the diffusion medium. The maximum in power density slightly increases with increasing the platinum loading (Fig. 8) but turns out in unacceptable values of the Pt-specific power density (Fig. 9).

4. Conclusions

In this work, we have utilized DLI-MOCVD to deposit ultra-low Pt loadings directly onto the microporous side of a commercial GDL. Two metal precursors, decomposing at different temperatures, have been tested. The higher temperature (320 °C) required to decompose Pt(cod) vs. Pt(X) (250 °C) facilitates growth of the mean Pt particle size. Hence, we observed a decrease of both the specific surface area and the roughness factor of the PEMFC electrodes for Pt(cod) vs. Pt(X). This means that not only the mass of Pt loaded onto the electrode but also the particle nanostructure is key-parameter to use Pt to the fullest possible extent. When using the best metal precursor Pt(X), homogeneous distribution of the Pt particles onto the carbon particles and low degree of agglomeration were observed (FEG-SEM). Both physical (TEM, XRD) and electrochemical techniques showed that the mean-particle size increases with increasing the Pt loading. Cross-sections slices of the home-made electrodes revealed that 90% of the Pt particles are contained in a region ca. 2–3 μm thick (TEM) close to the interface with the PEM. Impregnation with a diluted Nafion® solution and hot-pressing favor high utilization factors u_{Pt}. The electrocatalytic activity of the home-made electrodes was determined in liquid electrolyte (e.g. 0.5 M H$_2$SO$_4$) or in solid polymer electrolyte, e.g. in a fuel cell operating on pure H$_2$/O$_2$ or H$_2$/air and compared vs. that of a commercially available electrode (ELAT® LT140E-W/SI, BASF Fuel Cell Inc.). In liquid electrolyte, we noted an increase of the mass activity with decreasing the Pt loading (i.e. the Pt particle size), in agreement with the structure sensitivity of the ORR. Interestingly, using Pt(cod) or Pt(X) yields comparable MA for a given Pt particle size, showing no pollution of the catalytic sites. In solid polymer electrolyte, 80 °C and H$_2$/O$_2$ conditions, the cell voltage is under kinetic control up to 0.3 A cm^{-2} with apparent Tafel slopes ranging from 50 to 70 mV decade^{-1}. Interestingly, electrodes elaborated by DLI-MOCVD and containing more than 104 μg_{Pt} cm^{-2} performed better at the cathode in the region $j > 0.3$ A cm^{-2} than a commercial electrode containing 500 μg_{Pt} cm^{-2}, pointing towards larger effectiveness of the home-made electrodes. An optimum in power density was found for cathode Pt loadings of ~225 μg_{Pt} cm^{-2} in H$_2$/O$_2$ conditions. This translates into a Pt-specific power density of 0.6 g_{Pt} kW^{-1} with a non-optimized anode (500 μg_{Pt} cm^{-2}). In H$_2$/air conditions, additional mass-transport losses affect the polarization

curves in the low-current density region and the performances are comparable at 1 A cm^{-2} pointing towards facile mass-transport in our GDE. Due to the fast HOR kinetics, the anode operates within a few mV of the reversible potential and the Pt loading can be reduced to 35 μg_{Pt} cm^{-2} without any voltage loss. This study confirms that the Pt loading of the cathode fix the price of the MEA.

Acknowledgments

References

[1] P. Costamagna, S. Srinivasan, J. Power Sources 102 (2001) 242.
[2] H.A. Gasteiger, S.S. Kocha, B. Sompalli, F.T. Wagner, Appl. Catal. B 56 (2005) 9.
[3] K.C. Neyerlin, W. Gu, J. Jorne, H.A. Gasteiger, J. Electrochem. Soc. 154 (2007) B631.
[4] K.C. Neyerlin, W. Gu, J. Jorne, H.A. Gasteiger, J. Electrochem. Soc. 153 (2006) A1955.
[5] S. Mukerjee, S. Srinivasan, A.J. Appleby, Electrochim. Acta 38 (1993) 1661.
[6] P. Stonehart, P.N. Ross, Electrochim. Acta 21 (1976) 441.
[7] F. Gloaguen, F. Andolfatto, R. Durand, P. Ozil, J. Appl. Electrochem. 24 (1994) 863.
[8] F. Gloaguen, R. Durand, J. Appl. Electrochem. 27 (1997) 1029.
[9] T.R. Ralph, G.A. Hards, J.E. Keating, S.A. Campbell, D.P. Wilkinson, M. Davis, J. St Pierre, M.C. Johnson, J. Electrochem. Soc. 144 (1997) 3845.
[10] F. Maillard, M. Martin, F. Gloaguen, J.M. Léger, Electrochim. Acta 47 (2002) 3431.
[11] F. Maillard, S. Pronkin, E.R. Savinova, Handbook of Fuel Cells: Advances in Electrocatalysis, Materials, Diagnostics and Durability, vols. 5–6, John Wiley & Sons, Inc, New York, 2009, p. 91.
[12] O. Antoine, Y. Bultel, R. Durand, P. Ozil, Electrochim. Acta 43 (1998) 3681.
[13] S. Mukerjee, J. Appl. Electrochem. 20 (1990) 537.
[14] H.A. Gasteiger, J.E. Panels, S.G. Yan, J. Power Sources 127 (2004) 162.
[15] R.R. Passos, V.A. Paganin, E.A. Ticianelli, Electrochim. Acta 51 (2006) 5239.
[16] S. Donet, S. Mailley, L. Guetaz, C. Anglade, F. Emieux, E. Billy, Journées thématiques SFT-CEA Grenoble, 2008.
[17] S. Mailley, P. Capron, S. Thollon, T. Krebs, W.I.P. Organization, France, WO/2007/088292, 2007.
[18] S. Mailley, F. Sanchette, S. Thollon, F. Emieux, W.I.P. Organization, France, WO/2007/088291, 2007.
[19] P. Doppelt, C. Thurier, I.N.P.I., France, FR09/00165, 2009.
[20] A.J. Bard, L.R. Faulkner, Electrochemical Methods—Fundamentals and Applications, John Wiley & Sons, Inc., Weinheim, 2001.
[21] S. Trasatti, O.A. Petrii, J. Electroanal. Chem. 327 (1992) 353.
[22] G. Bergeret, P. Gallezot, in: G. Ertl, H. Knözinger, J. Weitkamp (Eds.), Handbook of Heterogeneous Catalysis, Wiley–VCH, Weinheim, 1997, p. 439.
[23] P. Brault, A. Caillard, A.L. Thomann, J. Mathias, C. Charles, R.W. Boswell, S. Escribano, J. Durand, T. Sauvage, J. Phys. D-Appl. Phys. 37 (2004) 3419.
[24] M. Cavarroc, A. Ennadjaoui, M. Mougenot, P. Brault, R. Escalier, Y. Tessier, J. Durand, S. Roualdès, T. Sauvage, C. Coutanceau, Electrochem. Commun. 11 (2009) 859.
[25] J. Goswami, P. Majhi, C.G. Wang, S.K. Dey, Proceedings of the 2nd Ferroelectric Workshop (FWPR-2001), San Juan, Puerto Rico, 2001, p. 13.
[26] J. Goswami, C.G. Wang, W. Cao, S.K. Dey, Chem. Vap. Depos. 9 (2003) 213.
[27] M.K. Debe, A.K. Schmoeckel, G.D. Vernstrom, R. Atanasoski, J. Power Sources 161 (2006) 1002.
[28] M.K. Debe, in: W. Vielstich, A. Lamm, H. Gasteiger (Eds.), Handbook of Fuel Cells: Fundamentals, Technology, and Applications, vol. 3, John Wiley & Sons, New York, 2003, p. 576.
[29] S.Y. Cha, W.M. Lee, J. Electrochem. Soc. 146 (1999) 4055.
[30] S. Hirano, J. Kim, S. Srinivasan, Electrochim. Acta 42 (1997) 1587.
[31] M. Alvisi, G. Galtieri, L. Giorgi, R. Giorgi, E. Serra, M.A. Signore, Surf. Coat. Technol. 200 (2005) 1325.
[32] M. Eikerling, A.A. Kornyshev, J. Electroanal. Chem. 453 (1998) 89.
[33] M. Eikerling, A.A. Kornyshev, J. Electroanal. Chem. 475 (1999) 107.
[34] M. Eikerling, A. Kornyshev, A. Kulikovsky, Fuel Cell Rev. 1 (2005) 15.
[35] Z.N. Farhat, J. Power Sources 138 (2004) 68.
[36] X. Cheng, B. Yi, M. Han, J. Zhang, Y. Qiao, J. Yu, J. Power Sources 79 (1999) 75.
[37] Z. Xie, T. Navessin, K. Shi, R. Chow, Q.P. Wang, D.T. Song, B. Andreaus, M. Eikerling, Z.S. Liu, S. Holdcroft, J. Electrochem. Soc. 152 (2005) A1171.
[38] O. Antoine, Y. Bultel, R. Durand, J. Electroanal. Chem. 499 (2001) 85.
[39] S. Mukerjee, J. McBreen, J. Electroanal. Chem. 448 (1998) 163.
[40] L. Genies, R. Faure, R. Durand, Electrochim. Acta 44 (1998) 1317.
[41] O. Antoine, R. Durand, J. Appl. Electrochem. 30 (2000) 839.
[42] N. Cunningham, E. Irissou, M. Lefevre, M.-C. Denis, D. Guay, J.-P. Dodelet, Electrochem. Solid-State Lett. 6 (2003) A125.
[43] A. Caillard, C. Charles, D. Ramdutt, R. Boswell, P. Brault, J. Phys. D-Appl. Phys. 42 (2009) 045207.